

Prediction of forming-limit curves of dual-phase steels based on a multiple length scale modelling approach considering material instabilities



R. Wesenjak^{a,b,*}, C. Krempaszky^{a,b}, E. Werner^b

^a Christian-Doppler-Laboratory of Material Mechanics of High Performance Alloys, Institute of Materials Science and Mechanics of Materials, Technische Universität München, Boltzmannstraße 15, 85748 Garching, Germany

^b Institute of Materials Science and Mechanics of Materials, Technische Universität München, Boltzmannstraße 15, 85748 Garching, Germany

ARTICLE INFO

Article history:

Received 5 May 2015

Received in revised form 15 September 2015

Accepted 17 September 2015

Available online 5 October 2015

Keywords:

Finite element simulation

Dual-phase steel

Nakajima-test

Material instability

Forming-limit curve

Micromechanics

Shear band

Abaqus FEA

ABSTRACT

In this contribution a decoupled sequential multiple length scale modelling approach to estimate forming-limit curves of dual-phase steels is presented. Two-dimensional Voronoï tessellated representative volume elements, based on the periodic microfield approach and under the assumption of plane stress are utilised to investigate the onset of material instabilities in the microstructure. Here, material instabilities, also termed as local stability problem or shear band, refer to a critical state of mechanical equilibrium where further strain increments do not lead to an increase of stress. To capture the influence of different microstructures and strength levels on shear band formation, DP500 and DP1000 dual-phase steels are analysed. The results of the micromechanical investigations are subsequently used to derive a damage criterion to predict material instabilities in finite element models of Nakajima-tests. Utilising this multi-scale approach enables the prediction of forming-limit curves which give a good estimation of the tendencies of experimentally determined curves.

© 2015 Elsevier B.V. All rights reserved.

1. Introduction

As a consequence of their microstructure, consisting of hard martensite grains embedded in a soft ferritic matrix, dual-phase steels exhibit low yield stress on the one hand and high tensile strength, high work hardening and high uniform elongation on the other hand. Due to their good formability and high strength, dual-phase steels are commonly used for complex cold worked structural elements and car body panels. The layout of such cold worked components requires data concerning strength and formability of the material. While strength properties like yield stress and tensile strength are usually assessed by tensile tests, forming limits in terms of the extent to which a material can be deformed safely by e.g. deep drawing or stretching are identified by Nakajima- (or Marciniak) tests. In this context a deformation is called safe when no localised necking or cracking occurs. The transition from safe to critical deformation is defined by the form-

ing limit curve (FLC), Fig. 1 [1]. In ductile materials like dual-phase steels, cracks are usually the consequence of shear fracture which in turn is related to formation of microvoids in areas subjected to high strains [2]. However, microvoids were also shown to influence localised necking prior to damage where the accumulation of voids leads to a softening in the structure and therefore contributes to localisation [3].

Besides to experimental investigations, a number of mechanical approaches, either on an empirical or physically motivated basis, were developed to predict the onset of damage and failure of Nakajima-specimen. Approaches assuming different kinds of continuum ductile fracture criteria are discussed by several authors [4–7]. The fracture criteria adopted in these approaches are usually related to specific (equivalent) stresses or strains. Prediction of FLCs based on damage induced by microvoids was studied by Uthaisangsuk et al. [8]. The authors use the Gurson–Tvergaard–Needleman (GTN) model [9,10] in order to analyse void formation in representative volume elements (RVE) of dual-phase and TRIP steels. The disadvantage of all mentioned approaches is, however, that specific material parameters are needed for calibration for the considered material which can be costly under certain circumstances. If the calibration is carried out for a specific

* Corresponding author at: Christian-Doppler-Laboratory of Material Mechanics of High Performance Alloys, Institute of Materials Science and Mechanics of Materials, Technische Universität München, Boltzmannstraße 15, 85748 Garching, Germany. Tel.: +49 89 289 15305.

E-mail address: wesenjak@wkm.mw.tum.de (R. Wesenjak).

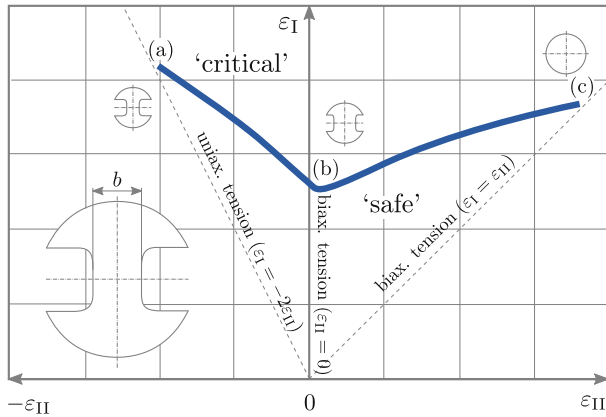


Fig. 1. Illustration of a forming-limit curve (FLC). A forming process is considered to be safe if the effective principal strains are below the FLC. The variables (a), (b) and (c) depict the three deformation paths UAT, PST and BAT. On the left side a Nakajima-specimen with shaft width b is depicted.

deformation path only, e.g. tensile strain, the results obtained from the calculations will accordingly agree with experimental findings for this specific deformation path only.

Another concept to predict FLCs is to describe damage as a consequence of localised necking. There are two well-known approaches. The first one was developed by Marciniak and Kuczynski [11] and has been extended in the last decades by several authors, an overview is given by Banabic [12]. The Marciniak–Kuczynski (M–K) model is based on the assumption that geometric imperfections in the material, e.g. fluctuation in sheet thickness due to manufacturing processes, will lead to localisation and failure. To follow this assumption in the modelling process, a notched sub-model is considered. The M–K model is suitable for the prediction of FLCs, however, it also needs to be calibrated for the considered material [12].

In the second approach the localisation is assumed to be the consequence of a material instability, which in this context is also referred to as shear band. A fundamental analysis of this problem was carried out by Hill [13], and its application to the prediction of FLCs can be reviewed in several contributions [14–17]. The advantage of this approach is that no specific damage or failure criterion is needed. The disadvantage, however, is that it is not possible to predict shear bands for principal strains $\varepsilon_I > 0$ and $\varepsilon_{II} > 0$ (biaxial tensile deformation) assuming plane stress [14]. Several approaches are proposed to address this restriction [14,15]. In this contribution, however, this restriction is addressed by accounting for the microstructure of the material. The contrast in strength between martensite and ferrite leads to an inhomogeneous distribution of stresses within the microstructure which triggers shear band formation even for macroscopic biaxial tensile deformation. Therefore our approach can be understood as a combination of the shear band analysis and the M–K approach where the heterogeneous microstructure represents an ‘imperfection’ similar to the notched sub-model employed by Marciniak [11].

The scope of this work is to estimate FLCs of the dual-phase steels DP500 and DP1000 using a decoupled sequential multi-scale modelling approach. For this purpose two-dimensional finite element models of the dual-phase microstructures under the assumption of plane stress are deformed along different linear deformation paths in the logarithmic strain space to analyse shear band formation. The plane stress approach was chosen in order to investigate shear band formation on the surface of a specimen since it is assumed that such shear bands can act as trigger for failure. Furthermore plane stress allows for a conservative estimation of the critical deformation state with

respect to shear band formation. The required equation for the shear band analysis is transformed into a bi-quadratic form which allows for a closed-form analytical solution. The findings from the micromechanical simulations are used to derive a damage criterion which is applied to predict shear band formation in finite element models of the Nakajima-test. Throughout this work the prediction of FLCs is restricted to three deformation paths, as shown in Fig. 1:

- (a) uniaxial tension (UAT),
- (b) biaxial tension with the principal strain, ε_{II} , being zero (also referred to as plane strain tension (PST)) and
- (c) biaxial tension (BAT).

In Section 2 the theoretical framework of material instabilities is discussed, the required equations for the plane stress approach are established and the applicability of the plane stress approach to this problem setting is discussed. The material parameters employed to describe the constitutive behaviour of the phases are summarised in Section 3. In Section 4 the micromechanical finite element model as well as the Nakajima-test model are introduced which are deployed in Section 5 to predict material instabilities on both length-scales.

2. Material instabilities

The term material instability refers to a material dependent phenomenon where the deformation exhibits an abrupt change from a smooth and homogeneous to a localised mode. The strain localisation, also referred to as shear band, is the result of a bifurcation¹ in the deformation path. As a consequence the material exhibits a critical mechanical equilibrium. The existence of a shear band does, however, not imply an unstable macroscopic mechanical equilibrium in the sense of abrupt failure of a specimen but represents a local weakening of the material [19].

The concept of describing material instabilities is based on the work of Hadamard [20], Thomas [21] and Hill [13,22] on the stability of elastic and elastic–plastic solids as well as the work of Hill [23] and Mandel [24] on acceleration waves in elastic–plastic solids (this survey of methods was taken from [25]). Further noticeable contribution to this topic were published by Hill, Rice and Rudnicki [13,25–28].

2.1. Bifurcation criterion

Fig. 2 shows a section of a homogeneous continuum, \mathcal{A} , in a critical mechanical equilibrium, where a shear band, $\partial\mathcal{A}$, has been formed. The continuum is considered to be subjected to a homogeneous velocity gradient, \dot{u}_{ij} , as well as an initially (prior to bifurcation) homogeneous stress state, P_{ij} , with P_{ij} denoting the first Piola–Kirchhoff stress tensor and \dot{P}_{ij} its time derivative. The vector $\mathbf{g} = g_i \mathbf{e}_i$ denotes the jump of the velocity gradient, being non-zero only within the shear band and $\mathbf{n} = n_i \mathbf{e}_i$ is the normal vector to the shear band.

If the deformation velocity-field in the continuum is continuous, at least prior to bifurcation, the velocity gradient within the shear band is for compatibility reasons restricted to the form [25,27,28]

$$\dot{u}_{ij}^{\partial\mathcal{A}} = \dot{u}_{ij}^{\mathcal{A}} + g_i n_j. \quad (1)$$

¹ Bifurcation here refers to the abrupt appearance of qualitatively different solutions as a consequence of a slight variation of parameters [18].

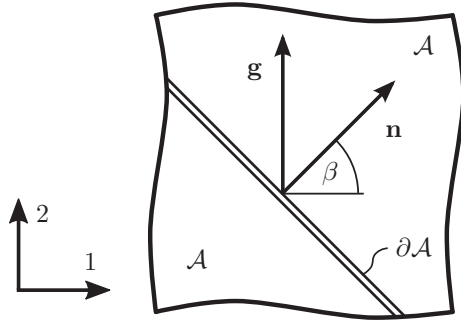


Fig. 2. Schematic representation of a shear band, ∂A . The vector $\mathbf{n} = n_i \mathbf{e}_i$ denotes the normal vector to the shear band and $\mathbf{g} = g_i \mathbf{e}_i$ the jump of the velocity gradient inside the shear band. The vectors $\mathbf{E} = \{\mathbf{e}_1, \mathbf{e}_2\}$ are the basis vectors of the vector space consisting of orthogonal unit vectors. The shear band, ∂A , separates the depicted section into two homogeneously deformed areas, A .

To account for rigid spins, the constitutive law of the continuum is expressed under consideration of the co-rotational Jaumann derivative of the Cauchy stress. This leads to the formulation [29,30]

$$\dot{P}_{ij} = \left(L_{ijkl} + \frac{1}{2} (\sigma_{ik} \delta_{jl} - \sigma_{il} \delta_{jk} - \sigma_{jl} \delta_{ki} - \sigma_{jk} \delta_{il}) \right) \dot{u}_{k,l}, \quad (2)$$

where δ_{ij} is the Kronecker-Delta and σ_{ij} the Cauchy stress tensor. The term

$$L_{ijkl} + \frac{1}{2} (\sigma_{ik} \delta_{jl} - \sigma_{il} \delta_{jk} - \sigma_{jl} \delta_{ki} - \sigma_{jk} \delta_{il}) := \hat{L}_{ijkl} \quad (3)$$

is subsequently denoted as co-rotational tangent stiffness tensor, \hat{L}_{ijkl} .

Consequently, the stress rate in the shear band follows

$$\dot{P}_{ij}^{\partial A} = \hat{L}_{ijkl}^{\partial A} \dot{u}_{k,l}^{\partial A} = \hat{L}_{ijkl}^{\partial A} (\dot{u}_{k,l}^A + g_k n_l), \quad (4)$$

and outside the shear band

$$\dot{P}_{ij}^A = \hat{L}_{ijkl}^A \dot{u}_{k,l}^A. \quad (5)$$

The equilibrium condition in terms of the material derivative of the first Piola–Kirchhoff stress, \dot{P}_{ij} , can be expressed by

$$(\dot{P}_{ij} - \dot{u}_k P_{ij,k})_{,i} = 0. \quad (6)$$

Since the stresses in the continuum are homogeneously distributed prior to bifurcation, the critical condition for the stress rate equilibrium at bifurcation is [25]

$$\dot{P}_{ij,i}^{\partial A} = \dot{P}_{ij,i}^A = 0, \quad (7)$$

resulting in the additional condition that the traction rate, \dot{t}_j , inside and outside the shear band is the same [25]:

$$\dot{t}_j^{\partial A} = \dot{t}_j^A \quad \text{or} \quad \dot{P}_{ij}^{\partial A} n_i = \dot{P}_{ij}^A n_i. \quad (8)$$

Inserting Eqs. (4) and (5) into Eq. (8) we obtain after rearranging

$$\hat{L}_{ijkl}^{\partial A} n_k n_l g_i = (\hat{L}_{ijkl}^A - \hat{L}_{ijkl}^{\partial A}) \dot{u}_{k,l}^A n_i. \quad (9)$$

Furthermore it is assumed that both co-rotational tangent stiffness tensors, \hat{L}_{ijkl}^A and $\hat{L}_{ijkl}^{\partial A}$, are equal at least prior to bifurcation and thus the right hand side of Eq. (9) vanishes. Hence the bifurcation criterion for arbitrary g_i has the form

$$\det(\hat{L}_{ijkl} n_k n_l) =: \det(Q_{ji}) = 0. \quad (10)$$

The tensor Q_{ji} is denoted as acoustic- or localisation tensor. If Eq. (10) is satisfied, the acoustic tensor has a zero eigenvalue at least

for one direction n_i , which entails that an increase of deformation does not lead to an increase of traction in at least one direction n_i .

2.2. Shear band analysis for plane stress

The homogeneous continuum, cf. Section 2.1, is considered to be two-dimensional assuming plane stress. Stress components are given in the principal axis system where index $()_I$ denotes the maximum and $()_{II}$ the minimum in-plane principal direction, respectively.

The material behaviour is described utilising the von Mises plasticity model assuming isotropic hardening and an associated flow rule. The tangent stiffness tensor within the deformed configuration can be written in the form [31]

$$L_{ijkl} = E_{ijkl} + C_t (D_{ij} (4G + 3K) - \delta_{ij} D_{pp} (2G - 3K)) (-D_{kl} (4G + 3K) + \delta_{kl} D_{qq} (2G - 3K)), \quad (11)$$

with the elasticity tensor [32]

$$E_{ijkl} = 2G \left(\frac{1}{2} (\delta_{il} \delta_{jk} + \delta_{jl} \delta_{ik}) + \frac{-2G + 3K}{4G + 3K} \delta_{ij} \delta_{kl} \right). \quad (12)$$

The variable C_t is an abbreviation for the term

$$C_t = \frac{9G^2}{(-27G^2 D_{pp} D_{qq}) (4G + 3K) + \hat{\sigma}^2 (3G + h) (4G + 3K)^2}, \quad (13)$$

with the yield stress

$$\hat{\sigma} = \sqrt{\sigma_I^2 - \sigma_I \sigma_{II} + \sigma_{II}^2}. \quad (14)$$

The variables G and K denote the shear and bulk modulus, respectively, h the work hardening and D_{ij} the deviatoric stress tensor, $D_{ij} = \sigma_{ij} - \frac{1}{3} \sigma_{kk} \delta_{ij}$. The co-rotational tangent stiffness tensor, \hat{L}_{ijkl} , can be obtained from Eq. (3). The shear band normal, n_i , is expressed as a function of the shear band angle, β , it encloses with the global 1-direction, Fig. 2,

$$\mathbf{n} = \begin{pmatrix} \cos \beta \\ \sin \beta \end{pmatrix}. \quad (15)$$

By inserting Eqs. (3), (11) and (15) into Eq. (10) we obtain after rearranging a biquadratic equation for β of the form

$$\det(Q_{ji}) = A \tan^4 \beta + B \tan^2 \beta + C = 0, \quad (16)$$

with the coefficients

$$A = (2G - (\sigma_I - \sigma_{II})) \left((-3K \sigma_{II} + 12KG^* - 4\sigma_{II} G^* + 4GG^*) \times (\sigma_I^2 - \sigma_I \sigma_{II} + \sigma_{II}^2) - (3G - 3G^*) (\sigma_I - \sigma_{II})^2 \sigma_{II} + K(3G - 3G^*) (-2\sigma_I + \sigma_{II})^2 \right),$$

$$B = \left((-3K - 4G^*) (\sigma_I - \sigma_{II})^2 - 6KG^* (\sigma_I + \sigma_{II}) + 16G^2 G^* + 8GG^* (6K - \sigma_I - \sigma_{II}) \right) (\sigma_I^2 - \sigma_I \sigma_{II} + \sigma_{II}^2) + (6G^2 - 6GG^*) \times (-2K(\sigma_I - 2\sigma_{II})(2\sigma_I - \sigma_{II}) + (\sigma_I - \sigma_{II})^2 (\sigma_I + \sigma_{II})) - (3G - 3G^*) \left((\sigma_I - \sigma_{II})^4 + 2K(\sigma_I^3 + \sigma_{II}^3) \right),$$

$$C = (2G + (\sigma_I - \sigma_{II})) \left((-3K \sigma_I + 12KG^* - 4\sigma_I G^* + 4GG^*) (\sigma_I^2 - \sigma_I \sigma_{II} + \sigma_{II}^2) - (3G - 3G^*) (\sigma_I - \sigma_{II})^2 \sigma_I + K(3G - 3G^*) (\sigma_I - 2\sigma_{II})^2 \right).$$

The variable G^* denotes the instantaneous shear modulus

$$G^* = \frac{Gh}{3G + h}. \quad (17)$$

By evaluating the discriminant of Eq. (16), information can be gained about the stability of a given mechanical equilibrium condition. If the discriminant is negative, $B^2 - 4AC < 0$, no real roots exist, i.e. $\forall \beta : \beta \in \mathbb{C}$. In this case the characteristic regime of the governing differential equation is elliptic and the mechanical equilibrium is considered to be stable. If $B^2 - 4AC \geq 0$, either four (hyperbolic regime) or two real roots (parabolic regime) exist and the mechanical equilibrium is considered to be critical. In this contribution however, the evaluation of roots is limited to whether real roots and therefore shear bands exist or not, that is when $\exists \beta : \beta \in \mathbb{R}$.

2.3. A note on the application of the two-dimensional approach

Shear bands are three-dimensional objects consisting of a shear plane and a shear direction. Although shear bands can therefore only be fully described in 3D space, we want to show here that a two-dimensional approach assuming plane stress can, in a reasonable way, be applied to predict shear bands.

In case of the UAT specimen the maximum shear strain is in-plane (since the maximum and minimum principal strains are in-plane), resulting in an in-plane shear band formation and therefore a two-dimensional approach assuming plane stress is feasible. In case of the other two deformation paths, PST and BAT, the maximum shear strain is not in-plane, however, exemplary for the PST specimen it is shown that a plane approach still results in satisfactory estimates of the critical deformation state and the in-plane shear band angle.

In Fig. 3 (left) a Nakajima-specimen is depicted. The shaft width, b , cf. Fig. 1, is chosen in a way that the specimen follows the deformation path PST during testing. A small section of the Nakajima specimen is shown in Fig. 3 (right). The surface of the specimen with the normal vector pointing in 3-direction exhibits plane stress (blue) and the plane perpendicular, with normal vector pointing in 2-direction exhibits plane strain (green). A shear plane (light-grey) is indicated which results from the orientation of the shear bands in the two planes. The orientation of the shear bands is expressed by the shear band angles β (in-plane) and γ (in thickness-direction).

In this example the orientation of the shear plane can be evaluated by calculating the shear band angles β and γ independently by conducting shear band analyses on two-dimensional unit cells assuming plane stress and plane strain, Fig. 4. For this reason a finite element analysis is carried out using the commercial software Abaqus Unified FEA® [33]. The material is considered to be mechanically homogeneous. The employed constitutive law is based on von Mises plasticity assuming isotropic behaviour,

utilising the yield curve depicted in Fig. 5 (top; curve ‘DP500 ferrite’). The relevant equations for the shear band analysis are derived in Section 2.2 for plane stress and in Appendix D for plane strain. The unit cells are loaded as depicted in Fig. 4 in order to mimic the conditions in the specimen as discussed in Fig. 3.

The results of the simulations are summarised in Table 1. The variables σ_1, σ_2 and σ_3 denote the stresses in 1, 2 and 3-direction respectively, ε_1 denotes the logarithmic strain in 1-direction and h the work hardening. The results of β and γ show, that the shear plane in the PST specimen lies approximately as depicted in Fig. 3 which agrees with experimental findings. However, according to the results in Table 1, shear bands appear in case of plane stress at significantly lower strains than in case of plane strain. Furthermore, the work hardening in case of plane stress is also significantly higher than in case of plane strain, where the work hardening for stress states $\sigma \ll G$ must be $h \approx 0$ for shear bands to form.

To validate the results, a shear band analysis was carried out on a homogeneous three-dimensional unit cell (3D PST), cf. Appendix E, assuming the same material behaviour. For this purpose an Abaqus user-material subroutine is implemented to estimate β and γ by numerical solution of Eq. (10) using an optimisation routine. The results of this finite element analysis, outlined in Table 1, show that the estimated shear band angles of 2D and 3D simulations correspond with each other. However, the critical strain values of ε_1 at which the shear band forms varies. In case of the three-dimensional and the plane strain simulations shear bands form at higher strains compared to the plane stress simulation.

This leads to the conclusion that shear band analyses assuming plane stress result in a realistic estimation of the in-plane shear band angle and a conservative estimation of the critical deformation state. The advantage of this approach, however, is the possibility for closed-form analytical solutions allowing for a more efficient implementation, e.g. as post-processing routine. In case of 3D analyses it is recommended to adopt an Abaqus user-material subroutine in order to reduce computational efforts.

2.4. Finite element realisation

The shear band analysis, i.e. evaluation of Eq. (16), is carried out as a post-processing routine utilising Abaqus/CAE [33]. Material parameters as well as current stresses and strains in each time step are obtained from the output database (*.odb) and the current hardening is calculated from the material input data according to the current equivalent plastic strain. To evaluate and visualise the results of the shear band analysis we introduce the shear band variable, Q^s , which is defined as

$$Q^s = \begin{cases} +1 & \text{if Eq. (16) is satisfied for } \exists \beta : \beta \in \mathbb{R}, \\ 0 & \text{else.} \end{cases} \quad (18)$$

In general, finite element simulations involving material instabilities have to be considered critical since the solution of

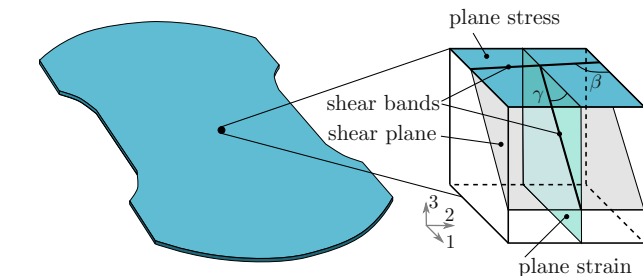


Fig. 3. Left: Specimen with a shaft width leading to the deformation path PST. Right: Small section of the specimen. The surface of the specimen, with the normal vector pointing in 3-direction exhibits plane stress (blue). The plane with the normal vector pointing in 2-direction exhibits plane strain (green). The angles of the estimated shear bands (assuming they already formed) are denoted by β and γ . The resulting shear plane is depicted in light-grey. (For interpretation of the references to colour in this figure legend, the reader is referred to the web version of this article.)

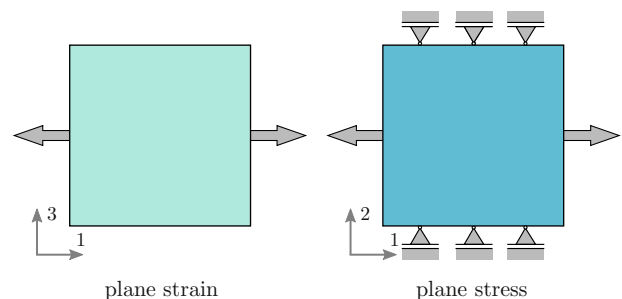


Fig. 4. Applied loading conditions of the plane strain (left) and plane stress (right) unit cell.

the balance equation loses its uniqueness, i.e. the characteristic regime of the governing equation is hyperbolic or parabolic, cf. Section 2.2. Referring to an affected finite element this implies that the rank of the element's stiffness matrix reduces due to a zero eigenvalue. However, a limited interpretation of the results at least at the bifurcation is possible since this effect is initially diminished by the assembly of the overall element stiffness matrix [19]. To maintain the ellipticity of the governing equation despite the occurrence of material instabilities the problem setting has to be reformulated. Several approaches are proposed in the literature, however, in terms of finite element analysis the most frequent approach is to utilise a finite element formulation with embedded displacement-discontinuity surfaces [34,35], but this is, however, not considered here.

3. Material characterisation

The strength of the material and the stress level influence shear band formation, cf. Eq. (3). Therefore the shear band analysis is carried out for two different virtual materials corresponding to

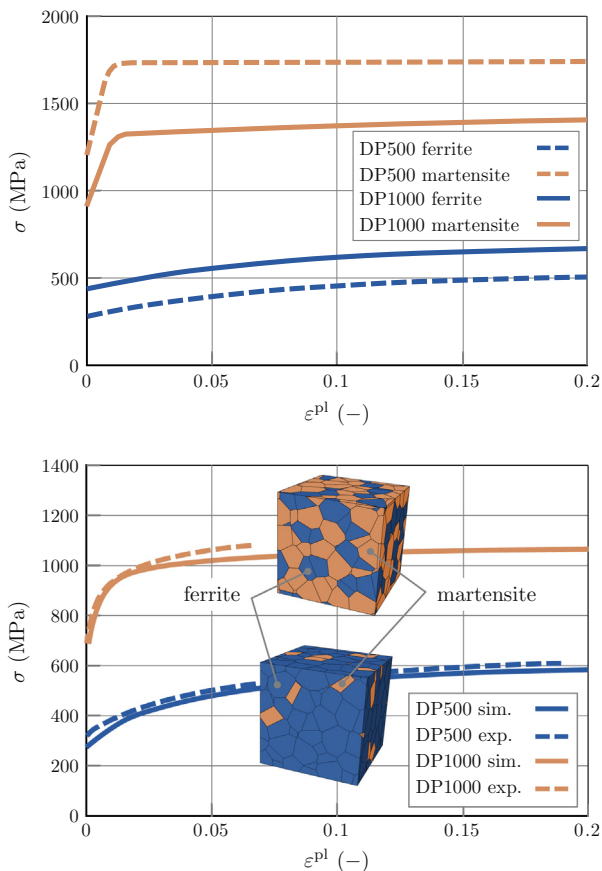


Fig. 5. Top: Ferrite (blue) and martensite (orange) flow curves for DP500 (dashed) and DP1000 (continuous) used as input for simulations, plotted as Cauchy stress, σ , against logarithmic plastic strain, ε^{pl} . Bottom: Flow curves of DP500 and DP1000 from experiments (dashed) and simulations (continuous). (For interpretation of the references to colour in this figure legend, the reader is referred to the web version of this article.)

Table 1
Results of the 2D and 3D simulations. All values are rounded.

	σ_1 (MPa)	σ_2 (MPa)	σ_3 (MPa)	ε_1 (-)	h (MPa)	β (°)	γ (°)
Plane strain	600	300	0	0.3	0	–	~45
Plane stress	570	285	0	0.15	360	~90	–
3D PST	600	300	0	0.3	~0	~90	~45

DP500 and DP1000 steels. The phase specific constitutive laws are based on the von Mises plasticity model assuming isotropic behaviour in the elastic as well as the plastic regime and isotropic hardening. Phase specific flow curves as input for the finite element analysis are generated on the basis of experimental data as described by Fillafer et al. [36]. The strength of the phases in his approach is depending on the mean grain size, d_{avg}^F , in case of ferrite and the mean hardness, h_{avg}^M , in case of martensite. The material parameters for DP500 and DP1000 employed in this work are summed up in Table 2.

Fig. 5 (top) shows the computed flow curves of ferrite and martensite. The resulting flow curves from a unit cell simulation as well as the experimental flow curves of DP500 and DP1000 are depicted in Fig. 5 (bottom).

4. Finite element models

In this section the set-up of the micromechanical RVE and the Nakajima-test is described. For the finite element discretisation and the solving of the resulting system of equations the commercial software Abaqus Unified FEA® is employed [33].

4.1. Nakajima-test model

The finite element model of the Nakajima testing device corresponds to the specifications in ISO 12004-2:2008 [1], Fig. 6. Blank holders as well as punch are modelled, however, blank holders are not used as clamping devices here but act as supporting devices to prevent warping of the specimen and to incorporate the forming radius. The specimen is fixed using displacement boundary conditions applied along the circumference. The forming process is induced by punch displacement. The contact surface between blank holder and specimen as well as punch and specimen is assumed to be frictionless. To ensure comparability with the micromechanical simulation results, the homogenised material for DP500 and DP1000 from Fig. 5 (bottom) is used as input for the simulations.

The finite element models of the Nakajima specimens, as shown in Fig. 6 (left), also correspond to the specifications in ISO 12004-2:2008. The shaft widths, b , of the Nakajima specimens correspond to the shaft widths of specimens reflecting the deformation paths UAT, PST and BAT in the experiment. For both, DP500 and DP1000, the deformation paths UAT and BAT are reflected by specimens with $b = 30$ mm and $b = R$, respectively. The specimen width reflecting the deformation path PST, however, differs for the two materials and is $b = 85$ mm in case of DP500 and $b = 70$ mm in case of DP1000. The specimens are modelled two-dimensional and are meshed using the Abaqus fully integrated finite-membrane-strain elements of type S4 with 5 integration points across the thickness. This is a general element type where stress in thickness-direction is zero and the strain in thickness-direction results from the Poisson's effect only [33].

4.2. Micromechanical finite element model

The two-dimensional micromechanical finite element model is based on the periodic microfield approach [37] assuming plane

Table 2

Phase fraction of martensite, contiguity of martensite and ferrite (cf. Appendix A.2), grain size of ferrite and hardness of martensite in steels DP500 and DP1000.

	Phase fraction	Contiguity		Grain size	Hardness
	p^M (%)	C^M (-)	C^F (-)	d_{avg}^F (μm)	h_{avg}^M (HV)
DP500	14	0.17		6.5	630
DP1000	64		0.25	2.1	500

(M...martensite; F...ferrite).

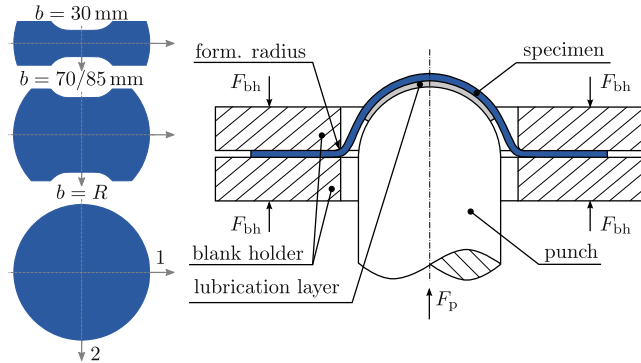


Fig. 6. Left: Illustration of the three Nakajima specimens with shaft-widths of $b = 30$, $b = 70/85$ mm (DP1000/DP500) and $b = R$. Right: Schematic representation of the Nakajima testing device (corresponding to the specifications in ISO 12004-2:2008 [1]).

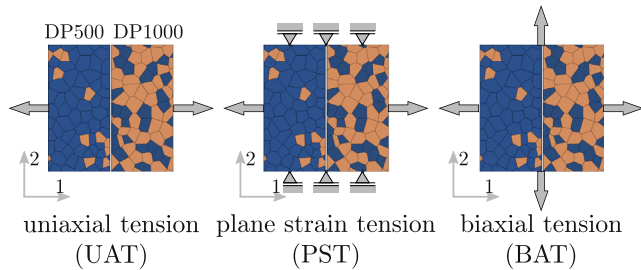


Fig. 7. Schematic representation of the applied loading in order to reflect the deformation paths (from left to right): uniaxial tension (UAT), plane strain tension (PST) and biaxial tension (BAT). The depicted unit cells show the microstructure of DP500 in the left half and DP1000 in the right half. Ferrite grains are shown in blue and martensite grains in orange. (For interpretation of the references to colour in this figure legend, the reader is referred to the web version of this article.)

stress. The employed unit cells consists of a geometrically periodic microstructure which is represented using a non-weighted Voronoï tessellation [38,39], Appendix A.1. This type of tessellation was proofed to be particularly suitable to approximate the grain structure of dual-phase steels [40]. Advantages of this approach compared to approaches where actual microstructures are represented are the ability of parametrisation as well as the low set-up time.

To allow for conclusions on the effective mechanical properties of the material based on micromechanical simulation results, the unit cell must be representative for the actual microstructure. This means that on the one hand the unit cell must include a sufficiently large number of grains and on the other hand the characteristics of the microstructure like phase fraction and distribution of the grains must be statistically representative for the material [41–43]. To identify the required number of grains in the unit cell a convergence study was conducted, Appendix B. It was found that for the employed two-dimensional unit cells a minimum number

of 100 Voronoï polygons (grains) is necessary. In this work unit cells with 125 grains are used. The morphology of the microstructure is modelled by assigning phases to the Voronoï grains based on the measured quantities of phase fraction and contiguity, cf. Table 2. For this purpose a so called *colouring algorithm* was developed in the form of an optimisation routine which was introduced in [36], Appendix A.2. As boundary condition for the geometrically periodic unit cell, extended periodic boundary conditions (b. c.) are applied [44]. Such boundary conditions allow for a smaller size of the unit cell compared to uniform displacement or uniform traction b. c. in order to obtain converged results [43]. Furthermore, the extended periodic b. c. do not necessitate a congruent mesh on opposing faces of the unit cell [44]. The micromechanical unit cell is discretised using the Abaqus element type CPS8 [33]. Fig. 7 shows the generated microstructures of DP500 (left half) and DP1000 (right half) as well as the applied loading.

5. Multi-scale FLC prediction

In the following section the set-up of the sequential multi-scale approach is presented. The micromechanical unit cells are used to derive a damage criterion which is then applied to finite element models of the Nakajima-tests.

5.1. Microstructure simulation

Simulation results obtained from the micromechanical unit cells are depicted in Fig. 8 for DP500 and in Fig. 9 for DP1000. The figures show effective stress–strain curves of the first Piola–Kirchhoff stress, P_{11} , plotted against the logarithmic strain, ε_{11} , in 1-direction for UAT (top), PST (centre) and BAT (bottom). Furthermore contour plots of the distribution of the hardening, h , the shear band variable, Q^s , as well as the maximum principal strain, ε_1 are shown. The contour plots depict the distribution of the field quantities for two distinct strains ε_{11}^1 and ε_{11}^2 . These strains were chosen in such a way that ε_{11}^1 represents the state of the unit cell when the first shear bands appear which is usually before reaching the tensile strength and ε_{11}^2 when a continuous shear band, i.e. a continuous band of elements where $Q^s = 1$, has formed across the unit cell.

For further discussion of Figs. 8 and 9 the terms ‘local shear band’ and ‘global shear band’ are introduced. Local shear band here refers to a critical mechanical equilibrium of an integration point, i. e. an integration point where $Q^s = 1$. The term global shear band refers to the whole ensemble of integration points in a critical mechanical equilibrium (local shear bands). Accordingly the term local shear band angle refers to the theoretical shear band angle, β , cf. Eq. (15), while the term global shear band angle refers to the orientation of the global shear band.

Fig. 8 shows that shear bands form in DP500, irrespective of the type of loading, primarily in regions of higher martensite concentration and at phase boundaries between ferrite and martensite. In these regions the ferritic matrix is subjected to higher strains leading to a lower hardening rate. Shear bands form before the tensile strength is reached. In the uniaxially loaded cell (UAT) global shear bands form at a global shear band angle of $\sim 54^\circ$. The local shear band angles are $\beta_{1,2,3,4} \approx \pm 55^\circ$, with $\beta_{1,2}$ and $\beta_{3,4}$ being two coincident real roots of Eq. (16). In case of PST one global shear band forms with a global shear band angle of $\sim 90^\circ$ while the local shear band angles are $\beta_{1,2,3,4} \approx \pm 87^\circ$. In case of the biaxially deformed unit cell two global shear bands form, each of them with an orientation of $\sim 90^\circ$ to the loading direction with a local shear band angle of $\beta_{1,2,3,4} \approx \pm 86^\circ$.

In DP1000, Fig. 9, shear bands primarily form at phase boundaries and in narrow regions of martensite embedded in local grain

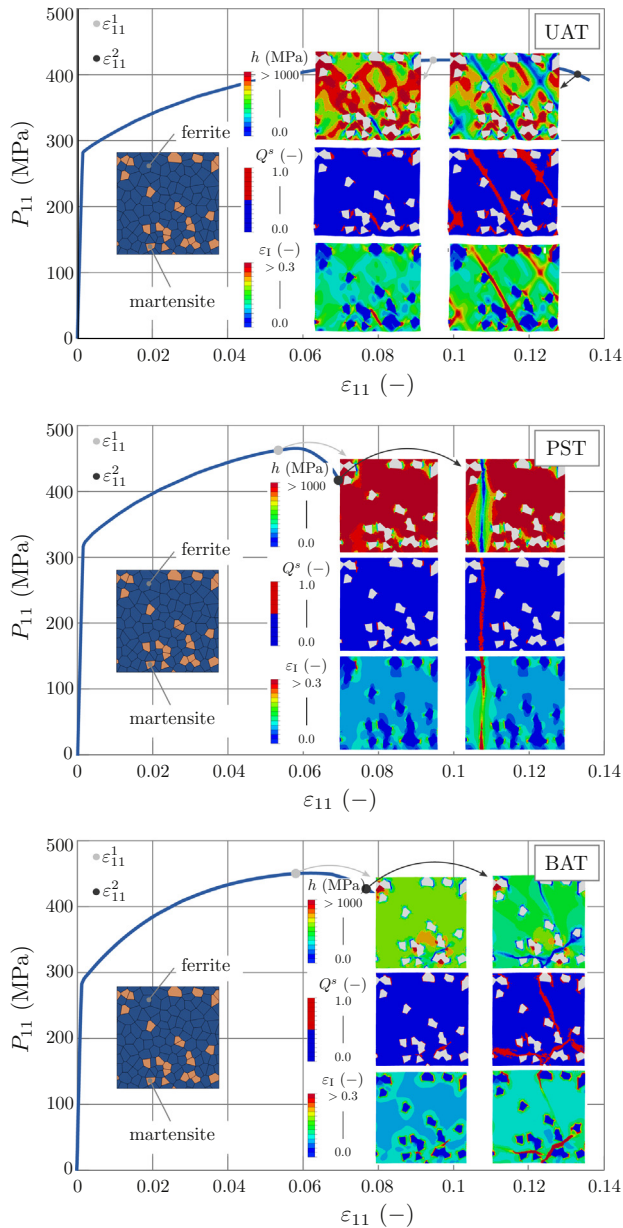


Fig. 8. Shear band analysis in a DP500 unit cell. From top to bottom: UAT, PST and BAT. The effective stress–strain curves are depicted in blue. Furthermore contour plots of the distribution of the hardening, h , the shear band variable, Q^* , and the maximum principal strain, ε_1 , are shown for two specific strains, $\varepsilon_{11}^{1,2}$. The white areas in the contour plots of Q^* represent martensite, the white colour indicates that martensite does not reach a critical state in DP500. (For interpretation of the references to colour in this figure legend, the reader is referred to the web version of this article.)

clusters of ferrite. In case of the uniaxially loaded (UAT) unit cell global shear bands form in two branches nearly perpendicular to the loading direction, while the local shear band angles are $\beta_{1,2,3,4} \approx \pm 55^\circ$. The orientation of the global shear band in the structure is dependent on the arrangement of ferrite, since ferrite is subjected to higher strains resulting in a lower hardening rate, as indicated by the contour plots of ε_1 and h . In case of the PST and the BAT loading global shear bands form at $\sim 90^\circ$ to the loading directions. The orientation of the global shear band is also dependent on the arrangement of ferrite. The local shear band angles are in case of PST $\beta_{1,2,3,4} \approx \pm 70^\circ$ and in case of BAT $\beta_{1,2,3,4} \approx \pm 83^\circ$.

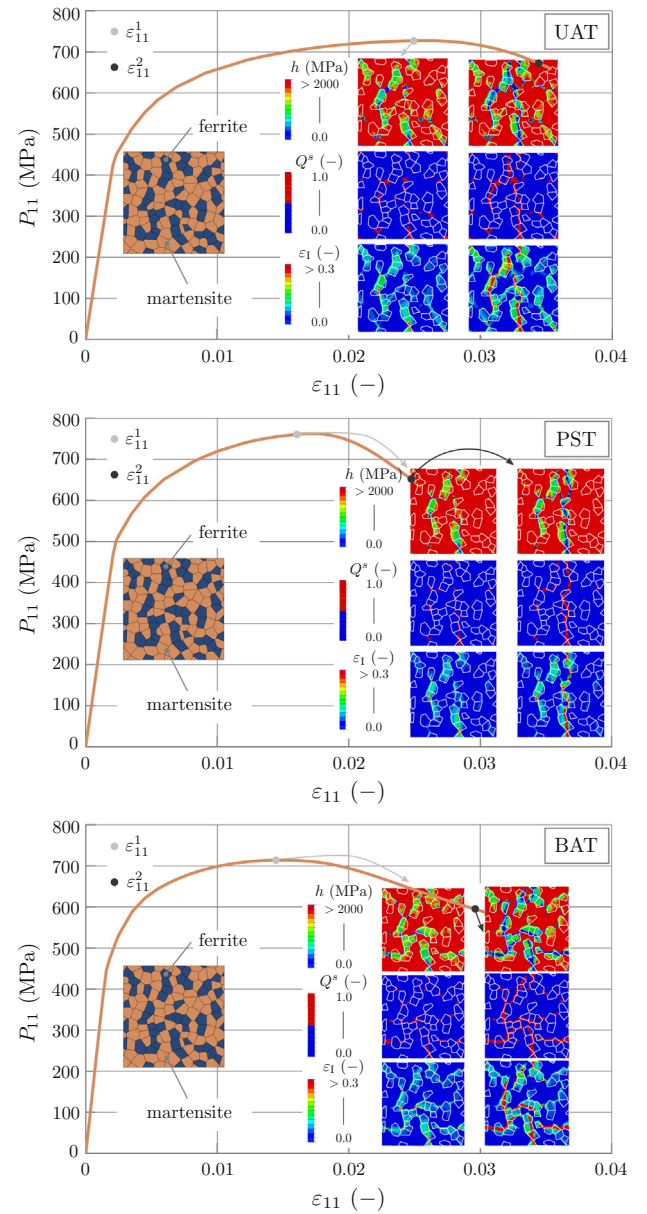


Fig. 9. Shear band analysis in a DP1000 unit cell. From top to bottom: UAT, PST and BAT. The effective stress–strain curves are depicted in orange. Furthermore contour plots of the distribution of the hardening, h , the shear band variable, Q^* , and the maximum principal strain, ε_1 , are shown for two specific strains, $\varepsilon_{11}^{1,2}$. Ferrite grain boundaries are indicated in white. (For interpretation of the references to colour in this figure legend, the reader is referred to the web version of this article.)

Since the presented shear band analysis is a pure post-processing routine rather than an element formulation, no interaction between shear bands and the surrounding structure takes place. For that reason the model is not able to return critical effective strains for which the micromechanical unit cell ‘fails’. However, to enable a comparison between the simulation and the experimental results it is assumed that the unit cell is damaged as soon as a continuous shear band forms (ε_{11}^2). Therefore the maximum and minimum homogenised principal strains are evaluated for each cell at ε_{11}^2 . This assumption also implies the existence of a continuous band of elements contributing a zero eigenvalue to the overall stiffness matrix which is finally leading to an overall decrease in stiffness.

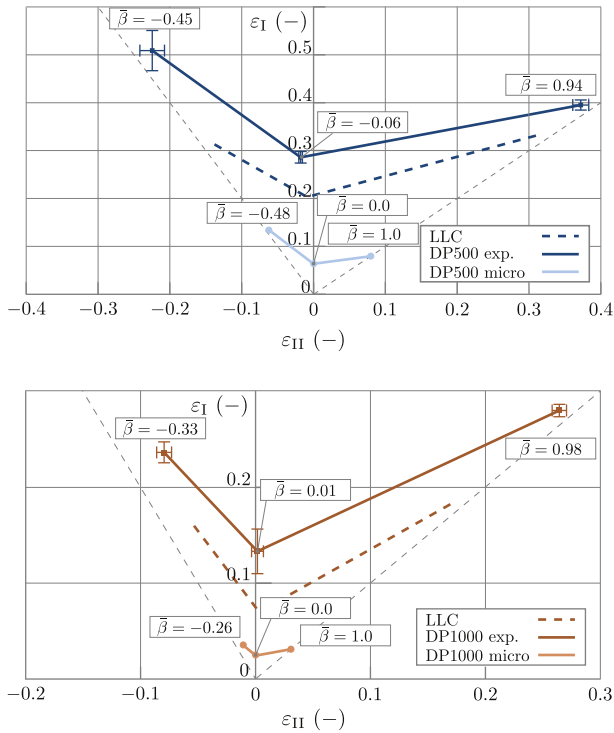


Fig. 10. Comparison of numerically (DP500/DP1000 micro) and experimentally (DP500/DP1000 exp.) determined FLCs. The variable $\bar{\beta}$ gives the ratio of second and first principal strain $\bar{\beta} = \varepsilon_{II}/\varepsilon_I$. The dashed lines depict the experimentally determined 'localisation-limit curves' (LLCs) which reflects principal strains within the Nakajima-specimens at the onset of strain localisation. Top: DP500. Bottom: DP1000.

The FLCs from the micromechanical simulations as well as the experimentally determined FLCs are shown in Fig. 10 for DP500 (top) and DP1000 (bottom). The experimentally determined FLCs are based on a total of 5 experiments for each shaft width b , cf. Fig. 6, and are depicted including standard deviation. Additionally to the FLCs a 'localisation-limit curve' (LLC) is derived from experimental results. The LLC reflects the maximum and minimum principal strains within the specimens at the onset of strain localisation. To estimate the LLC the evolution of the maximum principal strain, ε_I , along the 1-direction in the centre of the specimen was analysed for different punch displacements. Fig. 11 shows the evolution of ε_I exemplary for a DP500 specimen with shaft width $b = 30$ mm. Continuous curves ('bell-shaped') at small punch displacements indicate a homogeneous deformation while discontinuous curves ('taper-shaped') at higher punch displacements indicate the onset of strain localisation. Therefore the localisation-limit strains were estimated at the changeover of the curves from continuous to discontinuous behaviour.

The numerically estimated FLCs do not reflect experimental findings, neither in shape nor in magnitude. For instance, the estimated forming-limit of the uniaxially loaded cells correlate to the uniform elongation measured in tensile tests. In Nakajima-tests this forming limit is usually much higher due to a supporting effect of the geometry which the micromechanical model is not able to mimic.

5.2. Multi-scale simulation

The findings from the last section show that a limitation of the shear band analysis to the microscale, neglecting the overall structure of the specimen fails to predict experimentally determined LLCs. Furthermore, applying the shear band analysis to simulations

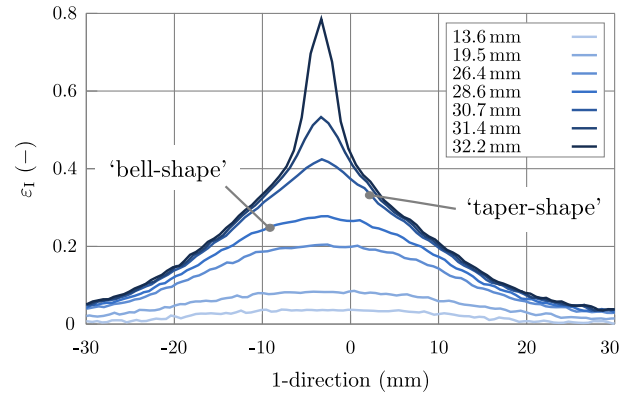


Fig. 11. Evolution of the maximum principal strain, ε_I , along the 1-direction in the reference system, exemplary shown for a DP500 specimen with shaft width $b = 30$ mm. The different colours of the lines indicate different punch displacements. (For interpretation of the references to colour in this figure legend, the reader is referred to the web version of this article.)

of the Nakajima-test assuming a homogeneous material neglecting the microstructure does not reflect experimental results either, especially for biaxial loading as depicted in Fig. 12. For this reason the critical strains estimated in the unit cells at ε_{II}^2 , Fig. 10, are used as a damage criterion for the Nakajima-test simulations. In this way the influence of the microstructure can be taken into account indirectly. The evaluation is carried out integration point wise. If the current strains of an integration point in the Nakajima-test model exceed the critical strains estimated by means of the micromechanical simulations (DP500/DP1000 micro; Fig. 10) the mechanical equilibrium of this integration point is considered to be critical.

In Fig. 12 a comparison between Nakajima-test simulations not taking into account the micromechanical damage criterion (left specimen) and the multi-scale simulations (right specimen) is depicted. The graphic shows contour plots of the distribution of the shear band variable with red areas for $Q^s = 1$. Each comparison (shaft width; material) is carried out at the same punch displacement. The contour plots of the specimens with $b = 30$ mm show similar shear band formation in simulations with (Q_{MS}^s) and without considering (Q^s) the micromechanical damage criterion while the specimens with shaft width $b = 70/85$ mm exhibit significantly smaller areas of global shear bands without considering the micromechanical damage criterion. In case of the round specimens no shear bands are predicted at the apex of the dome when the micromechanical damage criterion is not taken into account. As stated by Stören et al. [14], shear bands cannot be predicted for $\bar{\beta} = \varepsilon_{II}/\varepsilon_I > 0$ using the presented analysis in Section 2, if no further assumptions are made. Moreover, as can be seen in Fig. 12, the predicted size of the global shear band is also underestimated in case of $\bar{\beta} = 0$ without the micromechanical damage criterion. The consideration of the microstructure in the multi-scale approach here acts as the required 'imperfection' for shear band formation, comparable to the notched sub-model in the M-K approach [11]. While the morphology of the microstructure influences the position and orientation of the global shear band within the microstructure, cf. Section 5.1, the phase contrast is responsible for triggering shear band formation. However, the absolute difference in strength of the phases is insignificant as shown in Appendix C where a shear band analysis is carried out for unit cells with the same microstructure and different phase strength contrasts.

Fig. 13 shows FLCs based on the multi-scale modelling approach as well as the experimentally determined FLC and LLC for DP500

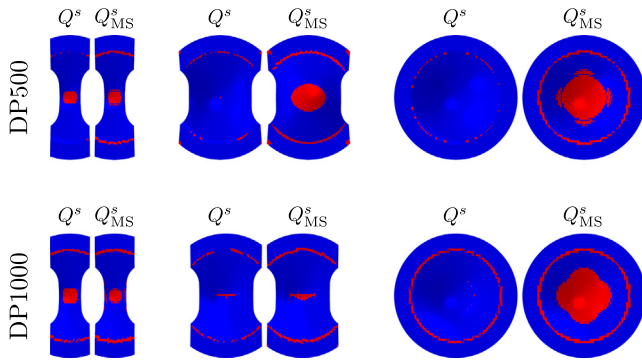


Fig. 12. Contour plots of the distribution of Q^s evaluated in Nakajima-test simulations without the micromechanical damage criterion (Q^s ; left specimen) and with the multi-scale approach (Q^s_{MS} ; right specimen). Red areas indicate elements exhibiting a critical mechanical equilibrium (shear band; $Q^s = 1$). Each comparison (shaft width; material) is carried out at the same punch displacement. (For interpretation of the references to colour in this figure legend, the reader is referred to the web version of this article.)

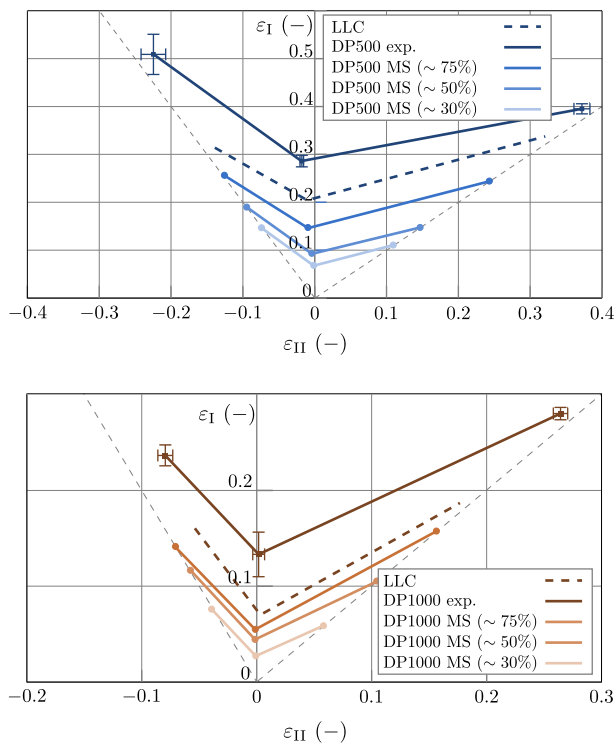


Fig. 13. Comparison of the experimentally determined FLCs (DP500/DP1000 exp.), the localisation-limit curves (LLCs) and the numerically estimated FLCs using the multi-scale approach (DP500/DP1000 MS). Top: DP500. Bottom: DP1000.

(top) and DP1000 (bottom). The FLCs from the multi-scale approach reflect principal strains in the finite element models of the Nakajima-specimens at states where the global shear band extends to ~30%, ~50% and ~75% of the specimen width. Strains exceeding the ones depicted by the line DP500/DP1000 MS (~75%) are leading to heavily distorted finite elements and therefore no evaluation is possible. By trend the shape of the curves DP500 MS/DP1000 MS lie between the LLC and the FLC. The presented multi-scale modelling approach seems to be suitable to predict the shape of FLCs although the magnitude of critical strains leading to shear band formation is underestimated in the simulations presented here at least for the evaluated shear band widths of up to 75%.

6. Summary and conclusions

In this contribution a decoupled sequential multi-scale approach to estimate FLCs of dual-phase steels DP500 and DP1000 was introduced. It was shown that a shear band analysis in plane stress finite element models of Nakajima-tests neglecting the influence of the microstructure does not lead to results comparable with experimental findings. Especially in case of the round Nakajima specimen the macroscopically homogeneous biaxial stress prevents shear band formation at the apex of the dome. To address this restriction, a damage criterion for Nakajima-test simulation models was derived on the basis of a two-dimensional model of the microstructure assuming plane stress.

In a first step shear band analyses were carried out for different loadings of the micromechanical models. It was found that the morphology of the microstructure influences the position and orientation of the global shear band within the microstructure while the phase strength contrast triggers shear band formation. The absolute magnitude of the phase contrast, however, is insignificant for shear band formation as long as the strengths of the phases differ.

In a second step critical principal strains (with respect to shear band formation) in the micromechanical models were evaluated when continuous shear bands had formed across the unit cells. These strains were subsequently used as a criterion for shear band formation in Nakajima-test simulation models. In this way the influence of the microstructure on shear band formation within the Nakajima-specimen is taken into account indirectly and altered the prediction of the onset of shear band formation significantly especially for specimens with wide shafts.

Utilising this sequential multi-scale approach it became possible to estimate the trend of the experimentally determined FLCs, however, the magnitudes of the critical principal strains were underestimated at least for the presented evaluation of global shear band width within the specimens of up to 75%. Three main reasons are believed to play an important role on the results of this contribution:

- For both the micromechanical and the Nakajima-test simulation model plane stress is assumed which underestimates mechanical field quantities on the one hand and overestimates the prediction of shear bands on the other hand.
- The shear band analysis is implemented as a post-processing routine and does not interact with the structure. Assumptions had to be made in accordance to transfer simulation results to an FLC. These assumptions might induce a certain error to the estimated critical principal strains.
- The estimation of the localisation-limit curves from the experiments is based on data of the 'bell-shaped curve' only. For a final conclusion of the capability of this approach to estimate FLCs it is necessary to find reliable localisation-limit curves directly from the experiment, e.g. by video evaluation.

Acknowledgements

The authors express their appreciation to their former colleagues B. Regener and T. Taxer, who contributed to this work by sharing code scripts for seed-point generation, tessellation and the extended periodic boundary conditions (xpbcc). We also thank A. Fillafer, who implemented several routines for the micromechanical research code employed in this work. Special thanks go to the voestalpine Stahl GmbH for conducting the Nakajima-tests and for providing the specimens. The authors gratefully acknowledge the financial support of the Christian Doppler Research Society (CDG) and the support of the TUM Graduate School.

Appendix A. Virtual microstructure generation

A.1. Geometrically periodic Voronoï tessellation

To generate a geometrically non-periodic two-dimensional Voronoï tessellation (Voronoi diagram) the space \mathcal{X} of a unit cell, $[0, 1] \times [0, 1] \subset \mathbb{R}^2$, with boundary $\Gamma_{\mathcal{X}}$ is populated with seed points, $p^k(x_i)$, with coordinates x_i using a so called *random sequential addition*² (RSA) algorithm [45]. The number of seed points, n_g , defines the number of Voronoï polygons (Voronoi grains) in the diagram. The distance d_i of a seed point to its neighbours is element of a truncated normal distribution with parameters

$$\mu_d = \frac{0.8}{\sqrt{n_g}} \quad \text{and} \quad \sigma_d = \frac{0.2}{\sqrt{n_g}} \quad (\text{A.1})$$

and the boundary condition $d = [0, 1/\sqrt{n_g}]$.

We consider the point set $P = \{p^1, \dots, p^{n_g}\} \subset \mathbb{R}^2$ with $2 \leq n_g < \infty$, $x_i^k \neq x_i^l$ for $k \neq l$ and $k, l \in I_{n_g} = \{1, \dots, n_g\}$. Then the space

$$X(p^k) = \{x_i \mid \|x_i - x_i^k\| \leq \|x_i - x_i^l\| \text{ for } k \neq l, l \in I_{n_g}\} \quad (\text{A.2})$$

is a 2-dimensional Voronoï-polygon, assigned to the seed point p^k and the set of polygons

$$\mathcal{X}(P) = \{X(p^1), \dots, X(p^{n_g})\} \quad (\text{A.3})$$

represents the Voronoï-diagram [39]. This approach will lead to an open, geometrically non-periodic Voronoï diagram, Fig. A.14 (left). To end up with a closed diagram, it is necessary to place further seed points outside of \mathcal{X} which act as artificial endpoints forcing the polygons within \mathcal{X} to be closed. If those additional artificial endpoints represent a periodic continuation of the initial set of seed points, P , the resulting Voronoï diagram is closed and geometrically periodic, Fig. A.14 (right).

A.2. Phase assignment (colouring process)

The phase assignment is carried out using a colouring algorithm developed by Fillafer et al. [36]. The colouring parameters employed to generate the virtual microstructure are the phase fractions of martensite, P^M , and ferrite, P^F , as well as the contiguity of the embedded phase, exemplary defined for martensite,

$$C^M = \frac{2S_V^{MM}}{2S_V^{MM} + S_V^{MF}}, \quad (\text{A.4})$$

where S_V^{MM} denotes the volume specific martensite/martensite grain boundary area and S_V^{MF} denotes the ferrite/martensite phase boundary area. Since the number of grains in this contribution is finite, the contiguity cannot be varied freely for a given phase fraction. Therefore the employed colouring algorithm uses tolerance limits for acceptance of a colouring pattern

$$|P^M - P_{\text{target}}^M| \leq P_{\text{tol}} \quad \text{and} \quad |C^M - C_{\text{target}}^M| \leq C_{\text{tol}} \quad (\text{A.5})$$

where P_{target}^M and C_{target}^M denote the desired colouring parameters, P_{tol} and C_{tol} denote the limit tolerances and P^M and C^M denote the actual colouring parameters in the virtual microstructure [36].

² The *random sequential addition* (also *adsorption*) (RSA) process is produced by randomly, irreversibly and sequentially placing nonoverlapping objects into a volume or area [45].

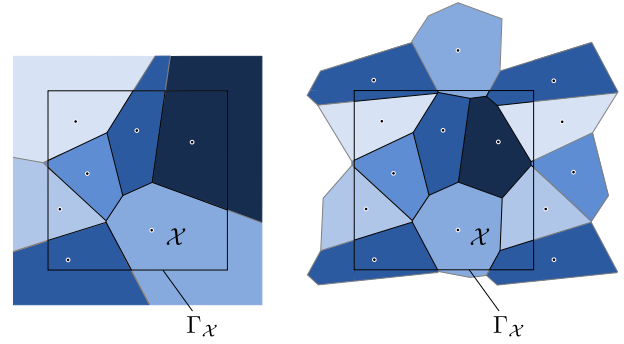


Fig. A.14. Voronoï-diagram with identical seed points $p^k(x_i)$ normally distributed in the space \mathcal{X} of a two-dimensional unit cell $[0, 1] \times [0, 1] \subset \mathbb{R}^2$ with the boundary $\Gamma_{\mathcal{X}}$. Left: Open, geometrically non-periodic Voronoï-diagram. Right: The periodic arrangement of the seed points outside of \mathcal{X} results in a closed, geometrically periodic Voronoï-diagram inside of \mathcal{X} .

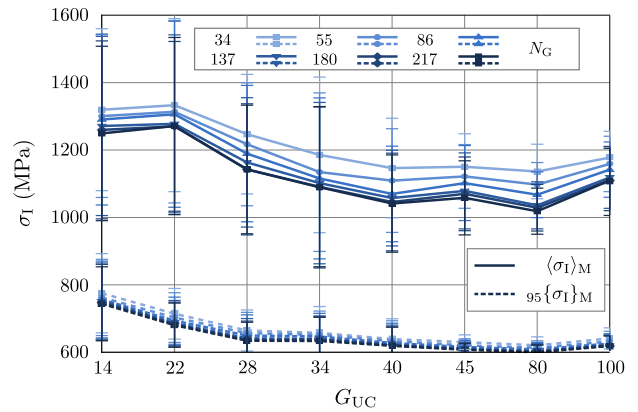


Fig. B.15. Convergence of the homogenised maximum principal stress, $\langle \sigma_I \rangle_M$, and the 95% quantile of the maximum principal stress, $95\{\sigma_I\}_M$, in martensite with respect to the number of grains within a unit cell, G_{UC} . Different mesh densities in terms of ‘degrees of freedom (DOFs) per grain’, N_G , were investigated to capture mesh dependency.

Appendix B. Convergence of effective mechanical properties

The convergence of effective mechanical properties is investigated with respect to the number of grains within a unit cell, $G_{UC} = \{14, 22, 28, 34, 40, 45, 80, 100\}$. Furthermore mesh dependency is studied by varying the mesh density in terms of ‘degrees of freedom (DOFs) per grain’, $N_G = \{34, 55, 86, 137, 180, 217\}$. For each G_{UC} and N_G a total number of 10 virtual microstructures were investigated. The unit cells are subjected to uniaxial displacement. Field quantities are evaluated at 20% engineering strain. Fig. B.15 shows the results exemplary for the homogenised maximum principal stress, $\langle \sigma_I \rangle_M$, (dashed) and the 95% quantile of the maximum principal stress, $95\{\sigma_I\}_M$, (continuous) in martensite.

For both depicted field quantities, differences in the results of unit cells with 45 grains and more are not significant. However, since the computational cost of such a two-dimensional approach is negligible (calculation time of the largest model considered $t_{\text{calc}} \approx 200$ s) a unit cell size of at least 100 grains is recommended.

Mesh density is also not significant in case of $\langle \sigma_I \rangle_M$. With respect to the results of $95\{\sigma_I\}_M$ a total number of $N_G \approx 130$ is found to be sufficient in this work.

Appendix C. Influence of the phase contrast on shear band formation

Fig. C.16 shows the results of a shear band analysis in a biaxially deformed unit cell with different phase contrasts. The flow curves

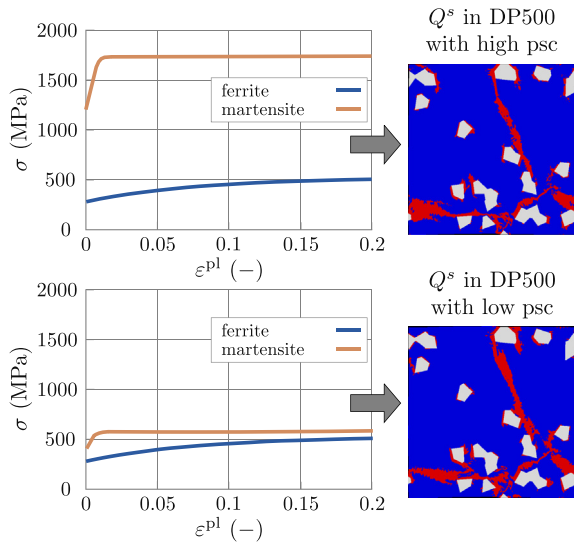


Fig. C.16. Shear band formation in a biaxially deformed unit cell with different phase strength contrasts (psc). Both cells exhibit comparable homogenised stress–strain relations. The graphic shows flow curves of martensite and ferrite as input for finite element simulations as well as contour plots of the distribution of the shear band variable Q^s within the unit cell. Top: Flow curves corresponding to the strength of ferrite and martensite in DP500 specimens, cf. Section 3. Bottom: Scaled flow curves in order to obtain a minimum phase contrast.

as input for simulation in the top graphic corresponds to the flow curves given in Section 3. The flow curves in the bottom graphic are scaled in a way that the phase contrast is minimised while keeping the resulting homogenised stress–strain relation in both unit cells comparable. It can be seen that shear band formation in both cells is similar, leading to the conclusion that the morphology of the microstructure markedly influences the position and orientation of the global shear bands. The magnitude of phase contrast however, is insignificant for shear band formation as long as the strengths of the phases differ.

Appendix D. Shear band analysis for plane strain

The derivation of the biquadratic equation for plane strain corresponds to the derivation for plane stress in Section 2.2. The tangent stiffness tensor within the deformed configuration can be written in the form [31]

$$L_{ijkl} = K\delta_{ij}\delta_{kl} + 2G\left(\frac{1}{2}(\delta_{il}\delta_{kj} + \delta_{jl}\delta_{ik}) - \frac{1}{3}\delta_{ij}\delta_{kl} - \frac{3G}{3G+h}\frac{D_{ij}D_{kl}}{\frac{2}{3}\hat{\sigma}^2}\right), \quad (D.1)$$

with the elasticity tensor [32]

$$E_{ijkl} = K\delta_{ij}\delta_{kl} + 2G\left(\frac{1}{2}(\delta_{il}\delta_{kj} + \delta_{jl}\delta_{ik}) - \frac{1}{3}\delta_{ij}\delta_{kl}\right). \quad (D.2)$$

Since $\sigma_{III} = (\sigma_I + \sigma_{II})/2$ in case of plane strain, the yield stress is given by

$$\hat{\sigma} = \frac{3}{4}\sqrt{(\sigma_I - \sigma_{II})^2}. \quad (D.3)$$

The variables G and K denote the shear and bulk modulus respectively, h the work hardening and D_{ij} the deviatoric stress tensor. The co-rotational tangent stiffness tensor, \hat{L}_{ijkl} , can be obtained from Eq. (3). By inserting Eqs. (3), (D.1) and (15) into Eq. (10) we obtain after rearranging a biquadratic equation for γ of the form

$$\det(Q_{jl}) = A \tan^4 \gamma + B \tan^2 \gamma + C = 0, \quad (D.4)$$

with the coefficients

$$A = (G + 3G^* + 3K - 3\sigma_{II})(2G - \sigma_I + \sigma_{II}),$$

$$B = (-4G^2 + 20GG^* - 3(\sigma_I - \sigma_{II})^2 + (6G - 12G^*)(-2K + \sigma_I + \sigma_{II})),$$

$$C = (G + 3G^* + 3K - 3\sigma_I)(2G + \sigma_I - \sigma_{II}).$$

Appendix E. Three-dimensional shear band analysis

The estimation of the shear band angles β and γ is carried out by solving Eq. (10) directly. The tangent stiffness tensor in the three-dimensional case is according to Eq. (D.1) and the elasticity tensor according to Eq. (D.2) with $i, j, k, l = 1, 2, 3$.

The von Mises yield stress is given by

$$\hat{\sigma} = \sqrt{\frac{1}{2}[(\sigma_I - \sigma_{II})^2 + (\sigma_{II} - \sigma_{III})^2 + (\sigma_{III} - \sigma_I)^2]} \quad (E.1)$$

and the shear band normal is expressed by spherical coordinates

$$\mathbf{n} = \begin{pmatrix} \cos \beta \cos \gamma \\ \cos \beta \sin \gamma \\ \sin \beta \end{pmatrix}. \quad (E.2)$$

References

- [1] ISO 12004-2:2008, *Metallic Materials – Sheet and Strip – Determination of Forming Limit Curves – Part 2: Determination of Forming Limit Curves in the Laboratory*, International Organization for Standardization, Geneva, Switzerland, 2008.
- [2] G. Avramovic-Cingara, C.A.R. Saleh, M.K. Jain, D.S. Wilkinson, *Metall. Mater. Trans. A* 40a (2009) 3117–3127, <http://dx.doi.org/10.1007/s11661-009-0030-z>.
- [3] C.C. Tasan, J.P.M. Hoefnagels, C. ten Horn, M.G.D. Geers, *Mech. Mater.* 41 (11) (2009) 1264–1276, <http://dx.doi.org/10.1016/j.mechmat.2009.08.003>.
- [4] H.N. Han, K.-H. Kim, *J. Mater. Process. Technol.* 142 (1) (2003) 231–238, [http://dx.doi.org/10.1016/S0924-0136\(03\)00587-9](http://dx.doi.org/10.1016/S0924-0136(03)00587-9).
- [5] M. Jain, J. Allin, D.J. Lloyd, *Int. J. Mech. Sci.* 41 (10) (1999) 1273–1288, [http://dx.doi.org/10.1016/S0020-7403\(98\)00070-8](http://dx.doi.org/10.1016/S0020-7403(98)00070-8).
- [6] Y.-W. Lee, J. Woertz, T. Wierzbicki, *Int. J. Mech. Sci.* 46 (5) (2004) 751–781, <http://dx.doi.org/10.1016/j.ijmecsci.2004.05.004>.
- [7] H. Takuda, K. Mori, N. Takakura, K. Yamaguchi, *Int. J. Mech. Sci.* 42 (4) (2000) 785–798, [http://dx.doi.org/10.1016/S0020-7403\(99\)00018-1](http://dx.doi.org/10.1016/S0020-7403(99)00018-1).
- [8] V. Uthaisangskul, U. Prahl, W. Bleck, *Int. J. Fract.* 157 (1–2) (2009) 55–69, <http://dx.doi.org/10.1007/s10704-009-9329-4>.
- [9] A.L. Gurson, *J. Eng. Mater. Technol.* 99 (1) (1977) 2–15, <http://dx.doi.org/10.1115/1.3443401>.
- [10] V. Tvergaard, A. Needleman, *Acta Metall.* 32 (1) (1984) 157–169, [http://dx.doi.org/10.1016/0001-6160\(84\)90213-X](http://dx.doi.org/10.1016/0001-6160(84)90213-X).
- [11] Z. Marciniak, K. Kuczynski, *Int. J. Mech. Sci.* 9 (9) (1967) 609–620, [http://dx.doi.org/10.1016/0020-7403\(67\)90066-5](http://dx.doi.org/10.1016/0020-7403(67)90066-5).
- [12] D. Banabic, A review on recent developments of Marciniak–Kuczynski model – a tribute to Professor Marciniak, *Tech. rep.*, Research Centre on Sheet Metal Forming, Technical University of Cluj Napoca, Cluj Napoca, Romania, 2010.
- [13] R. Hill, *J. Mech. Phys. Solids* 6 (3) (1958) 236–249, [http://dx.doi.org/10.1016/0022-5096\(58\)90029-2](http://dx.doi.org/10.1016/0022-5096(58)90029-2).
- [14] S. Stören, J.R. Rice, *J. Mech. Phys. Solids* 23 (6) (1975) 421–441, [http://dx.doi.org/10.1016/0022-5096\(75\)90004-6](http://dx.doi.org/10.1016/0022-5096(75)90004-6).
- [15] K. Hashiguchi, A. Protasov, *Int. J. Plast.* 20 (10) (2004) 1909–1930, <http://dx.doi.org/10.1016/j.ijplas.2003.11.018>.
- [16] B. Haddad, F. Abed-Meraim, T. Balan, *Int. J. Plast.* 25 (10) (2009) 1970–1996, <http://dx.doi.org/10.1016/j.ijplas.2008.12.013>.
- [17] M. Ben Bettaieb, F. Abed-Meraim, *Int. J. Plast.* 65 (2015) 168–190, <http://dx.doi.org/10.1016/j.ijplas.2014.09.003>.
- [18] P. Blanchard, *Differential Equations*, third ed., Thomson Brooks/Cole, Belmont, CA, 2006.
- [19] H. Baaser, *Anmerkungen zur Simulation von entfestigendem Materialverhalten*, Habilitation, TU Darmstadt, 2004.
- [20] J. Hadamard, *Leçons sur la propagation des ondes et les équations de l'hydrodynamique*, first ed., Librairie Scientifique, Paris, 1903.
- [21] T.Y. Thomas, *J. Math. Mech.* 7 (3) (1958) 291–322, <http://dx.doi.org/10.1002/zamm.19620420426>.
- [22] R. Hill, *J. Mech. Phys. Solids* 5 (3) (1957) 153–161, [http://dx.doi.org/10.1016/0022-5096\(57\)90001-7](http://dx.doi.org/10.1016/0022-5096(57)90001-7).

- [23] R. Hill, *J. Mech. Phys. Solids* 10 (1) (1962) 1–16, [http://dx.doi.org/10.1016/0022-5096\(62\)90024-8](http://dx.doi.org/10.1016/0022-5096(62)90024-8).
- [24] J. Mandel, in: J. Kravtchenko, P. Sirieys (Eds.), *Rheology and Soil Mechanics/Rhéologie et Mécanique des Sols*, Int. Union Theor. Appl. Mech., Springer, Berlin, Heidelberg, 1966, pp. 58–68, http://dx.doi.org/10.1007/978-3-642-46047-0_5.
- [25] J.R. Rice, J.W. Rudnicki, *Int. J. Solids Struct.* 16 (7) (1980) 597–605, [http://dx.doi.org/10.1016/0020-7683\(80\)90019-0](http://dx.doi.org/10.1016/0020-7683(80)90019-0).
- [26] R. Hill, J.W. Hutchinson, *J. Mech. Phys. Solids* 23 (4) (1975) 239–264, [http://dx.doi.org/10.1016/0022-5096\(75\)90027-7](http://dx.doi.org/10.1016/0022-5096(75)90027-7).
- [27] J.W. Rudnicki, J.R. Rice, *J. Mech. Phys. Solids* 23 (6) (1975) 371–394, [http://dx.doi.org/10.1016/0022-5096\(75\)90001-0](http://dx.doi.org/10.1016/0022-5096(75)90001-0).
- [28] J.R. Rice, in: W.T. Koiter (Ed.), *Proceedings of the 14th IUTAM Congress on Theoretical and Applied Mechanics*, North-Holland Publishing Company, Delft, Nederlande, 1976, pp. 207–220.
- [29] R. Hill, *Adv. Appl. Mech.*, vol. 18, Elsevier, 1979, pp. 1–75.
- [30] H. Petryk, *Arch. Comput. Meth. Eng.* 4 (2) (1997) 111–151, <http://dx.doi.org/10.1007/BF03020127>.
- [31] W.F. Chen, D.J. Han, *Plasticity for Structural Engineers*, first ed., Springer New York, New York, NY, 1988.
- [32] H. Eschenauer, W. Schnell, *Elastizitätstheorie I: Grundlagen, Scheiben und Platten*, second ed., Bibliographisches Institut, Mannheim, 1986.
- [33] Dassault Systèmes Simulia Corporation, *Abaqus Manual*, v6.11, 2011.
- [34] C. Miehe, J. Schröder, *Arch. Appl. Mech.* 64 (4) (1994) 267–285, <http://dx.doi.org/10.1007/BF00789125>.
- [35] J. Oliver, A.E. Huespe, M.D.G. Pulido, E. Samaniego, *Int. J. Numer. Meth. Eng.* 56 (7) (2003) 1051–1082, <http://dx.doi.org/10.1002/nme.607>.
- [36] A. Fillafer, C. Krempaszky, E. Werner, *Mater. Sci. Eng.: A* 614 (2014) 180–192, <http://dx.doi.org/10.1016/j.msea.2014.07.029>.
- [37] H. Böhm, *A short introduction to basic aspects of continuum micromechanics*, ILSB Report 206, ILSB, TU Wien, 1998.
- [38] G. Voronoï, *Journal für die reine und angewandte Mathematik* 134 (1908) 198–287.
- [39] A. Okabe, *Spatial Tessellations: Concepts and Applications of Voronoï Diagrams*, second ed., Wiley, Chichester, 2000.
- [40] E. Werner, T. Siegmund, H. Weinhandl, F.D. Fischer, *Appl. Mech. Rev.* 47 (1994) 231–240, <http://dx.doi.org/10.1115/1.3122817>.
- [41] R. Hill, *J. Mech. Phys. Solids* 11 (5) (1963) 357–372, [http://dx.doi.org/10.1016/0022-5096\(63\)90036-X](http://dx.doi.org/10.1016/0022-5096(63)90036-X).
- [42] M. Ostoj-Starzewski, X. Du, Z. Khisaeva, W. Li, in: T. Chandra, K. Tsuzaki, M. Militzer, C. Ravindran (Eds.), *THERMEC*, Pfäffikon, Switzerland, Trans Tech Publications, Ltd., 2006, pp. 201–206, <http://dx.doi.org/10.4028/www.scientific.net/MSF.539-543.201>.
- [43] K. Terada, M. Hori, T. Kyoya, N. Kikuchi, *Int. J. Solids Struct.* 37 (16) (2000) 2285–2311, [http://dx.doi.org/10.1016/S0020-7683\(98\)00341-2](http://dx.doi.org/10.1016/S0020-7683(98)00341-2).
- [44] T. Taxer, *Finite Element Simulation of Porous Nickel-Base Superalloys on Multiple Length Scales*, Dissertation, TU München, 2012.
- [45] S. Torquato, *Random Heterogeneous Materials Microstructure and Macroscopic Properties*, first ed., Springer New York, New York, NY, 2002.